



# Zn<sub>x</sub>Cd<sub>1-x</sub>Se nanoparticles decorated ordered mesoporous ZnO inverse opal with binder-free heterojunction interfaces for highly efficient photoelectrochemical water splitting

Yusheng Zeng<sup>a</sup>, Tingting Yang<sup>a</sup>, Chuanhao Li<sup>b</sup>, Anjian Xie<sup>a</sup>, Shikuo Li<sup>a,b,\*</sup>, Miaomiao Zhang<sup>a</sup>, Yuhua Shen<sup>a,\*</sup>

<sup>a</sup> Lab of Clean Energy & Environmental Catalysis, AnHui Province Key Laboratory of Chemistry for Inorganic/Organic Hybrid Functionalized Materials, Institute of Physical Science and Information Technology, School of Chemistry and Chemical Engineering, Anhui University, Hefei, 230601, PR China

<sup>b</sup> Guangdong Provincial Key Laboratory of Environmental Pollution Control and Remediation Technology, Sun Yat-sen University, Guangzhou, 510006, PR China



## ARTICLE INFO

### Keywords:

ZnO/Zn<sub>x</sub>Cd<sub>1-x</sub>Se  
Heteroepitaxial growth  
Heterojunction interface  
Inverse opal  
Photoelectrochemical water splitting

## ABSTRACT

Well-defined porous heteronanostructures with broad light absorption range and efficient charge transfer are the key challenges towards developing efficient photoanodes for photoelectrochemical (PEC) water splitting. Herein, we reported a facile template and continuous ion exchange method to fabricate three-dimensional ordered mesoporous (3DOM) ZnO/Zn<sub>x</sub>Cd<sub>1-x</sub>Se inverse opal with binder-free heterojunction interfaces on F-doped SnO<sub>2</sub> glass. The heteroepitaxial growth of Zn<sub>x</sub>Cd<sub>1-x</sub>Se shell layer on ZnO inverse opal skeleton surface provided favorable type-II band alignment, low interfacial resistance, and high visible light absorption. As expected, the optimized 3DOM ZnO/Zn<sub>x</sub>Cd<sub>1-x</sub>Se inverse opal achieved a significant saturated photocurrent density of 24.76 mA cm<sup>-2</sup> at 1.23 V versus a reversible hydrogen electrode (RHE) in 0.25 M Na<sub>2</sub>S and 0.35 M Na<sub>2</sub>SO<sub>3</sub> aqueous solution under AM 1.5 G simulated solar light irradiation (100 mW cm<sup>-2</sup>), which is 25 times higher than that of the pristine ZnO (0.99 mA cm<sup>-2</sup> at 1.23 V versus RHE) photoanode. The maximum photoconversion efficiency reached 10.64% for the optimized 3DOM ZnO/Zn<sub>x</sub>Cd<sub>1-x</sub>Se inverse opal at an applied potential of 0.52 V versus RHE, an about 22.63 times increase relative to that of the pristine ZnO inverse opal (0.47% at 0.61 V versus RHE). In addition, the photostability of the optimized 3DOM ZnO/Zn<sub>x</sub>Cd<sub>1-x</sub>Se inverse opal photoanode was also greatly improved in the electrolyte solution, 82.6% initial value was maintained even after 3000 s continuous light illumination without any protective coating layer. Such prominent PEC performances of the as-prepared 3DOM ZnO/Zn<sub>x</sub>Cd<sub>1-x</sub>Se inverse opal can be ascribed to the improved visible light harvesting and enhanced charge separation/collection efficiency. This work provides a fundamental insight to design the efficient photoanode for high performance water splitting.

## 1. Introduction

Photoelectrochemical (PEC) water splitting, utilizing solar energy for hydrogen and oxygen production, has been regarded as a promising technique to address the current energy issue [1–3]. The solar-to-hydrogen (STH) conversion efficiency is crucial important for large-scale developing the solar hydrogen practical application. The highest STH efficiency of 16.2% has been reported to date using a PEC water splitting system [4]. Theoretical studies have predicted the maximum efficiency of 23–32% for a designed semiconductor nanostructured electrode [5,6]. The high STH conversion efficiency requires an effective

separation of photogenerated charge carriers and their rapid transport to the semiconductor interface [7]. To pursue the effective charge separation, three-dimensional (3D) inverse opal nanostructure has been developed for boosting the efficiency [8–10]. The inverse opal structures with periodic inter-connected macropores and significant photon effect are most competitive in charge collection and light harvesting [8,11,12]. However, the inherent disadvantage of the single material obstacles the application of inverse opal in photocatalysis due to the unsatisfactory performance. Tuning inverse opal properties via component design and interfacial engineering are triggering more and more interest.

\* Corresponding authors at: Lab of Clean Energy & Environmental Catalysis, AnHui Province Key Laboratory of Chemistry for Inorganic/Organic Hybrid Functionalized Materials, Institute of Physical Science and Information Technology, School of Chemistry and Chemical Engineering, Anhui University, Hefei, 230601, PR China.

E-mail addresses: [lishikuo@ahu.edu.cn](mailto:lishikuo@ahu.edu.cn) (S. Li), [s\\_yuhua@163.com](mailto:s_yuhua@163.com) (Y. Shen).

Heterojunction structured inverse opals have shown favorable advantages in suppressing charge recombination and enhancing the overall photocatalytic activity. The single material is hard to possess both the narrow bandgap and proper band positions. Use a large band gap semiconductor as skeleton to couple with a small band gap semiconductor in inverse opals would obtain a more negative conduction band level, and the electrons can be easily injected from the small band gap semiconductor into the large band gap semiconductor [13,14]. The compact phase contact is crucial important to reduce the interfacial resistances for charge rapid transfer and separation at the heterojunction [9,15,16]. As a n-type semiconductor, ZnO with a wide bandgap (3.2 eV) has been well-investigated for a photoanode due to its good photoactivity, high electron mobility, nontoxicity, and relatively low cost [17–19]. Many narrow bandgap semiconductors have been developed to combine with ZnO to form heterojunction structures to enhance the STH conversion efficiency, such as CdS [20,21], CdSe [22,23] and CdTe [24]. In particular, ZnO/CdSe heterostructures with type-II band alignment are well known for the effective charge separation [25]. Various ZnO/CdSe nanostructures including nanowire [26], nanotube [27] and hierarchical structure [28] were thus being designed for PEC application. Although much progress has been achieved over the recent years, it remains a great challenge to construct ZnO/CdSe nanostructure with well-defined mesoporous framework and well-distributed heterojunctions. And for many composite nanostructures, interfacial resistances between the solid phases is usually existed; and this binder may restrict electron transfer and seriously affect stability [29]. Therefore, it is highly expected to prepare highly ordered ZnO/CdSe inverse opals with favorable interfacial heterojunction to direct charge transfer for efficient PEC water splitting.

Herein, we developed three-dimensional ordered mesoporous (3DOM) ZnO/Zn<sub>x</sub>Cd<sub>1-x</sub>Se inverse opal with binder-free heterojunction interface via continuous ion exchange reactions grown on F-doped SnO<sub>2</sub> glass. By incorporating Zn<sub>x</sub>Cd<sub>1-x</sub>Se as photosensitizer on ZnO inverse opal surface, an “antenna” is created that can harvest more photons for the heterostructures. Heteroepitaxial growth of Zn<sub>x</sub>Cd<sub>1-x</sub>Se shell on ZnO surface with type-II band alignment has the advantages of superior charge transport across the solid phase interface and low interfacial resistance. And the 3DOM architecture provides sufficiently active surface area to react with the electrolyte for PEC water splitting. As a result, the optimized ZnO/Zn<sub>x</sub>Cd<sub>1-x</sub>Se inverse opal achieved a maximum photocurrent density of 24.76 mA cm<sup>-2</sup> at 1.23 V (vs. RHE) in 0.25 M Na<sub>2</sub>S and 0.35 M Na<sub>2</sub>SO<sub>3</sub> aqueous solution under AM 1.5 G simulated sunlight (100 mW cm<sup>-2</sup>), which is the highest value ever reported to date for the ZnO/CdSe composites. In addition, the ZnO/Zn<sub>x</sub>Cd<sub>1-x</sub>Se inverse opal photoanode exhibited dramatically enhanced IPCE and excellent stability. To the best of our knowledge, it is seldom reported 3DOM ZnO/Zn<sub>x</sub>Cd<sub>1-x</sub>Se inverse opal photoanode for PEC water splitting. The high charge separation efficiency depends on the type-II band alignment, and the binder-free heterojunction interface in the 3DOM inverse opals, the mechanism of which is understood from electrochemical analysis. This work might be important for providing useful protocol to prepare nanostructured photoanodes for PEC water splitting.

## 2. Experimental

### 2.1. Synthesis of 3DOM ZnO/Zn<sub>x</sub>Cd<sub>1-x</sub>Se inverse opal via continuous ion exchange method

All chemicals in our experiments were of analytical grade and used as received without further purification. Fluorine-doped tin oxide (FTO) glass substrates were bought from Zhuhai Kaivo Electronic Components Co., Ltd (12 Ω cm<sup>-2</sup>) with a thickness of 1.2 mm and dimensions of 1.0 × 2.0 cm. Deionized water (resistivity over 18 MΩ cm) from a Millipore Q water purification system was used in all experiments. Before experiments, FTO glass was ultrasonically cleaned in piranha

solution (V<sub>H2SO4</sub>: V<sub>H2O2</sub> = 3: 1) to make the surfaces hydrophilic, and blow-dried with nitrogen before use. The 3DOM ZnO/Zn<sub>x</sub>Cd<sub>1-x</sub>Se inverse opals grown on FTO glasses were synthesized via the following reactions. The high 3DOM ZnO inverse opals were first prepared on FTO glasses according to our previous reported method [9]. 0.05 mol NaBH<sub>4</sub> and 0.025 mol Se were respectively dissolved in 100 ml deionized water under slow magnetic stirring (30 rpm) until the solution become clear and transparent. Then the ZnO inverse opal substrate was vertically immersed into the above mixed solution at 60 °C for 4 h. After that, the substrate was taken out from the reaction and washed thoroughly by ethanol and deionized water. The substrate became from light blue to yellow, indicating the anion exchange reaction occurred. Subsequently, the substrate was immersed into 100 ml 0.025 mol CdCl<sub>2</sub> solution, and then the reaction solution was sealed and heated to 120 °C for 8 h. After the cation exchange, the deep brown substrate was taken out from the reaction and cleaned by ethanol and deionized water. Finally, it was dried under vacuum at 60 °C for further characterization and use. The experiments in 100 ml 0.0125, and 0.0375 mol CdCl<sub>2</sub> solution for the cation exchange were also performed under the similar procedures.

### 2.2. Synthesis of pure CdSe nanoparticles

50 ml CdCl<sub>2</sub> (25 mM) aqueous solution was mixed with 50 ml Na<sub>2</sub>SeSO<sub>3</sub> (25 mM) aqueous solution in a 200 ml glass bottle, which was then sealed and heated in an electric oven at 120 °C for 8 h. After reaction, the sample centrifuged and cleaned by deionized water for further use.

### 2.3. Characterization

Scanning electron microscopy (SEM) images were recorded using a Zeiss Supra 40 scanning electron microscope at an acceleration voltage of 5 kV. Transmission electron microscope (TEM) images were obtained by JEOL JEM-2010-TEM with an accelerating 70 voltage of 200 kV. A powder X-ray diffraction (XRD) pattern was analyzed on a Philips X'Pert PRO SUPER X-ray diffractometer equipped with graphite-monochromated Cu Kα radiation ( $\lambda = 1.54056 \text{ \AA}$ ). The transient time resolved PL decay measurements were recorded on a FS5 fluorescence spectrometer (Edinburgh Instruments, UK), and the solutions of all the samples were excited by a 325 nm laser. UV-vis spectra were measured using a spectrophotometer (Hitachi U-4100) equipped with an integrating sphere. X-ray photoelectron spectroscopy (XPS) was recorded using an ESCALab MKII spectrometer with Al Ka (1486.6 eV) as the X-ray source. All of the data acquisition and processing were accomplished using XPS PEAK software. Inductively Coupled Plasma-Atomic Emission Spectrometry (ICP-AES) were obtained by iCAP 7400 Duo. Brunauer–Emmett–Teller (BET) measurements were achieved through nitrogen absorption-desorption isotherms on a V-Sorb2800 P analyzer at 77 K.

### 2.4. Photoelectrochemical measurements

The photoelectrochemical measurements were performed on CHI 660E (CH Instrument Inc., Shanghai) workstation with a three-electrode electrochemical system in a solution containing 0.25 M Na<sub>2</sub>S and 0.35 M Na<sub>2</sub>SO<sub>3</sub> (pH 12.5) under AM 1.5 G simulated sunlight illumination (100 mW cm<sup>-2</sup>), which was provided by a solar simulator (300 W Xe lamp, Beijing China Education Au-light Co., Ltd). The intensity of the solar simulator light was calibrated to 100 mW cm<sup>-2</sup> using calibrated silicon solar cells. The as prepared ZnO/Zn<sub>x</sub>Cd<sub>1-x</sub>Se inverse opals, Ag/AgCl (3 M KCl) and Platinum mesh were used as the working electrode, reference electrode, and counter electrode, respectively. The available electrode area immersed in the electrolyte solution was fixed to 1 × 1 cm. The electrolyte was stirred and purged with Ar gas before the measurements. All linear-sweep voltammetry (LSV) scan

rates were settled into  $10 \text{ mV s}^{-1}$ . Amperometric I – t curves were obtained under chopped light irradiation with on/off interval of 20 s at an applied potential of 1.23 V versus reversible hydrogen electrode (RHE). And the long-term stability experiments were carried out at 1.23 V vs RHE. Electrochemical impedance spectroscopy (EIS) was performed by using of Zahner IM6 (Zahner Elektrik, Kronach, Germany) at a frequency range of 10 kHz to 0.1 Hz with an amplitude of 10 mV in the dark. Photocurrent spectra were acquired at an applied potential of 1.23 V vs. RHE with 1 nm steps in the range of 365–800 nm using a Zahner IM6 equipment with LED lamps. The wavelength dependent incident photon-to-current efficiency (IPCE) could be calculated according to the following equation:

$$\text{IPCE}(\%) = [(1240 \times i_{ph})/(\lambda \times P_{in})] \times 100\%$$

where  $i_{ph}$  is the photocurrent density ( $\text{mA cm}^{-2}$ ),  $\lambda$  is the wavelength (nm) of incident radiation,  $P_{in}$  is intensity of the incident light ( $\text{mW cm}^{-2}$ ) with selected wavelength irradiated on the electrode. The measured potentials vs. Ag/AgCl (3 M KCl) were converted to the RHE scale using the following relationship:

$$E_{\text{RHE}} = E_{\text{Ag/AgCl}} + 0.059pH + E_{\text{Ag/AgCl}}^0$$

## 2.5. Hydrogen evolution measurements

The evolution of hydrogen by PEC water splitting was carried out in an air-tight reactor connected to an online gas chromatograph (GC2014C, Shimadzu) using a thermal conductivity detector, a 5 Å molecular sieve column, and Ar as the carrier gas. The ZnO, and ZnO/Zn<sub>x</sub>Cd<sub>1-x</sub>Se inverse opal photoanodes were biased at 1.23 V vs. RHE in a stirred aqueous solution of 0.35 M Na<sub>2</sub>SO<sub>3</sub> and 0.25 M Na<sub>2</sub>S (pH 12.5) under AM 1.5 G simulated sunlight. For Faradaic efficiency, it was calculated by the following equation:

$$\text{Faradaic efficiency}(\%) = nzF/Q \times 100\%$$

where z is the number of electron gain-loss (for example,  $2\text{H}^+$  back to H<sub>2</sub>, z is 2), n is amount of substance of H<sub>2</sub> (mol), F is the Faraday constant (96 500 C mol<sup>-1</sup>), and Q is the total charge.

## 3. Results and discussion

The fabrication procedures of 3DOM ZnO/Zn<sub>x</sub>Cd<sub>1-x</sub>Se inverse opals are schematically illustrated in Fig. 1a. As seen, the procedures can be divided into three steps, i.e., i) self-assembly multilayers of PS spheres onto FTO substrates as template, ii) fabrication of 3DOM ZnO inverse opals by removal of the PS spheres, and iii) heteroepitaxial growth of Zn<sub>x</sub>Cd<sub>1-x</sub>Se nanoparticles on ZnO inverse opal surface by successive ion exchange reactions. The typical SEM images of ZnO inverse opals are displayed in Figure S1, where 3D periodically ordered structures and continuous voids are clearly observed. The diameter of the cavity size is ca. 200 nm, which is slightly higher than that of the PS spheres template (Figure S2). After Zn<sub>x</sub>Cd<sub>1-x</sub>Se sensitization, the heteroepitaxial growth of Zn<sub>x</sub>Cd<sub>1-x</sub>Se shell layer are uniformly distributed on the ZnO inverse opal surface without any pores clogging, keeping the periodical characteristic very well (Fig. 1b, c). Apparently, the wall thickness increased from 30 nm to 40 nm, suggesting the ion exchange reactions occurred [30]. Fig. 1d displays the uniformly 3D periodically porous character of the as-prepared inverse opals with a thickness of ca. 20 μm. This core/shell configuration is further confirmed by TEM images (Fig. 2a, b), in which the high-quality 3DOM structure is composed of interconnected macropores within a nanocrystalline skeleton, in good agreement with the SEM observations. In comparison with Figure S3, the pore diameter of ZnO/Zn<sub>x</sub>Cd<sub>1-x</sub>Se inverse opal is obviously smaller than that of pristine ZnO inverse opal. HRTEM image (Fig. 2c and Figure S3) shows the presence of Zn<sub>x</sub>Cd<sub>1-x</sub>Se shell with a thickness of ca. 10 nm. The lattice fringes with a *d*-spacing of 0.19 nm is ascribed to the (002) plane of ZnO. The fringes with lattice spacing of 0.25 nm, 0.33 nm are assigned

to (102) plane of CdSe, and (111) plane of ZnSe, respectively. It confirms the co-existence of ZnSe and CdSe phase in the shell. Moreover, the compact interfacial contact between the core/shell phases provides persuasive proof that the Zn<sub>x</sub>Cd<sub>1-x</sub>Se phases are directly transformed from the ZnO cores rather than being randomly deposited on the surface. The binder-free heterojunctions lead to unimpeded electron transfer through the interface. The coating of Zn<sub>x</sub>Cd<sub>1-x</sub>Se phases on ZnO surfaces was further identified by the energy dispersive X-ray (EDX) spectra (Figure S4) and EDS mapping analysis (Fig. 2d-g), in which the Zn, and O elements are distributed in the core region, while Cd and Se are located homogeneously in the whole inverse opal shell. In addition, the elemental mass contents of Zn, O, Cd and Se of the as-prepared sample are 6.50 wt.%, 5.01 wt.%, 29.4 wt.% and 59.09 wt.%, respectively. Such a 3DOM core/shell nanostructure with binder-free heterojunction interface will maximize the surface area and charge rapid transfer, thus expected to enhance the PEC activity.

To further investigate the structure and chemical environment of the as-fabricated 3DOM ZnO/Zn<sub>x</sub>Cd<sub>1-x</sub>Se inverse opals, X-ray diffraction (XRD) patterns, X-ray photoelectron spectroscopy (XPS) was performed. As displayed in Fig. 3a, all of the diffraction peaks in the patterns of ZnO inverse opal samples could be indexed to the wurtzite phase of ZnO (JCPDS no. 36-1451;  $a = 0.47 \text{ nm}$ ,  $c = 0.32 \text{ nm}$ ), corresponding to the (100), (002), (101), (102), (103), and (200) reflections at  $31.8^\circ$ ,  $34.4^\circ$ ,  $36.3^\circ$ ,  $47.5^\circ$ ,  $62.9^\circ$ , and  $66.4^\circ$ , respectively [31]. After heteroepitaxial growth of Zn<sub>x</sub>Cd<sub>1-x</sub>Se shell layer, the new peaks appear at  $23.8^\circ$ ,  $25.3^\circ$ ,  $27.0^\circ$ ,  $41.9^\circ$ ,  $45.7^\circ$ , and  $49.6^\circ$  match well with the planes of (100), (002), (101), (110), (103), and (112) of hexagonal CdSe (JCPDS file no. 65-3415), respectively [32]. Noticeably, no ZnSe peaks were detected in the XRD pattern, possibly owing to its low component contents. The surface chemical states of the as-prepared typical 3DOM ZnO/Zn<sub>x</sub>Cd<sub>1-x</sub>Se inverse opals were carried out by XPS analysis. The survey spectra (Figure S5a) show the presence of zinc (3.5 atomic%), cadmium (15.98 atomic%), oxygen (35.96 atomic%), selenium (17.88 atomic%) and small amounts of remnant carbon (26.68 atomic%). In order to further confirm the real composition of the Zn<sub>x</sub>Cd<sub>1-x</sub>Se shell, ICP-AES measurements were also performed. The result shows that the molar ratio of Zn/Cd in the shell is 0.13/0.87, corresponding to a chemical formula of ZnO/Zn<sub>0.13</sub>Cd<sub>0.87</sub>Se of the typical sample. The binding energies of Cd 3d<sub>5/2</sub> (405.1 eV) and Cd 3d<sub>3/2</sub> (411.9 eV) peaks (Fig. 3b) indicates the presence of Cd<sup>2+</sup> states in the sample [33]. The Se 3d core level spectra as shown in Figure S5b consist of a doublet located a binding energies of 53.9 and 54.7 eV, which can be assigned to the Se 3d<sub>5/2</sub> and Se 3d<sub>3/2</sub> of Se<sup>2-</sup> in CdSe, respectively [34]. A distance between Cd 3d<sub>5/2</sub> and Se 3d<sub>5/2</sub> peaks is 351.21 eV matching the value reported for CdSe nanocrystals. The Zn 2p core level spectra were shown in Fig. 3c. The binding energies of 1021.5 and 1044.6 eV are in according with Zn 2p<sub>3/2</sub> and Zn 2p<sub>1/2</sub>, respectively. After growth of CdSe shell layer, the peak of Zn 2p red shift to 1021.8 and 1044.9 eV, suggesting the possible charge transfer between ZnO and CdSe. The decrease in peak intensity further indicates the coating of Zn<sub>x</sub>Cd<sub>1-x</sub>Se on ZnO surface, in agreement with the TEM observations. The XPS spectrum of oxygen (Fig. 3d) shows that the binding energy of O 1 s on the 3D ZnO/Zn<sub>x</sub>Cd<sub>1-x</sub>Se inverse opal has shifted to about 530.9 eV compared with 3DOM ZnO at 530 eV, due to the introduction of Zn<sub>x</sub>Cd<sub>1-x</sub>Se. The fact that Zn 2p and O 1 s peak positions in the 3DOM ZnO/Zn<sub>x</sub>Cd<sub>1-x</sub>Se inverse opal had slight shift compared with those in pure ZnO sample indicates that a charge or energy transfer occurred after the formation of the heterojunction.

The surface area and pore structure are significant factors for the photocatalytic applications. The N<sub>2</sub> adsorption-desorption measurements exhibit that the optimized 3DOM ZnO/Zn<sub>x</sub>Cd<sub>1-x</sub>Se inverse opal sample has a large Brunauer–Emmett–Teller (BET) surface area of  $46.19 \text{ m}^2 \text{ g}^{-1}$  with an average pore size of ca. 5.04 nm as shown in Fig. 4a, b. The optical properties of as-prepared 3DOM ZnO inverse opal, and 3DOM ZnO/Zn<sub>x</sub>Cd<sub>1-x</sub>Se inverse opals were investigated by diffuse reflectance UV-vis spectra (DRS UV-vis). As shown in Fig. 4c

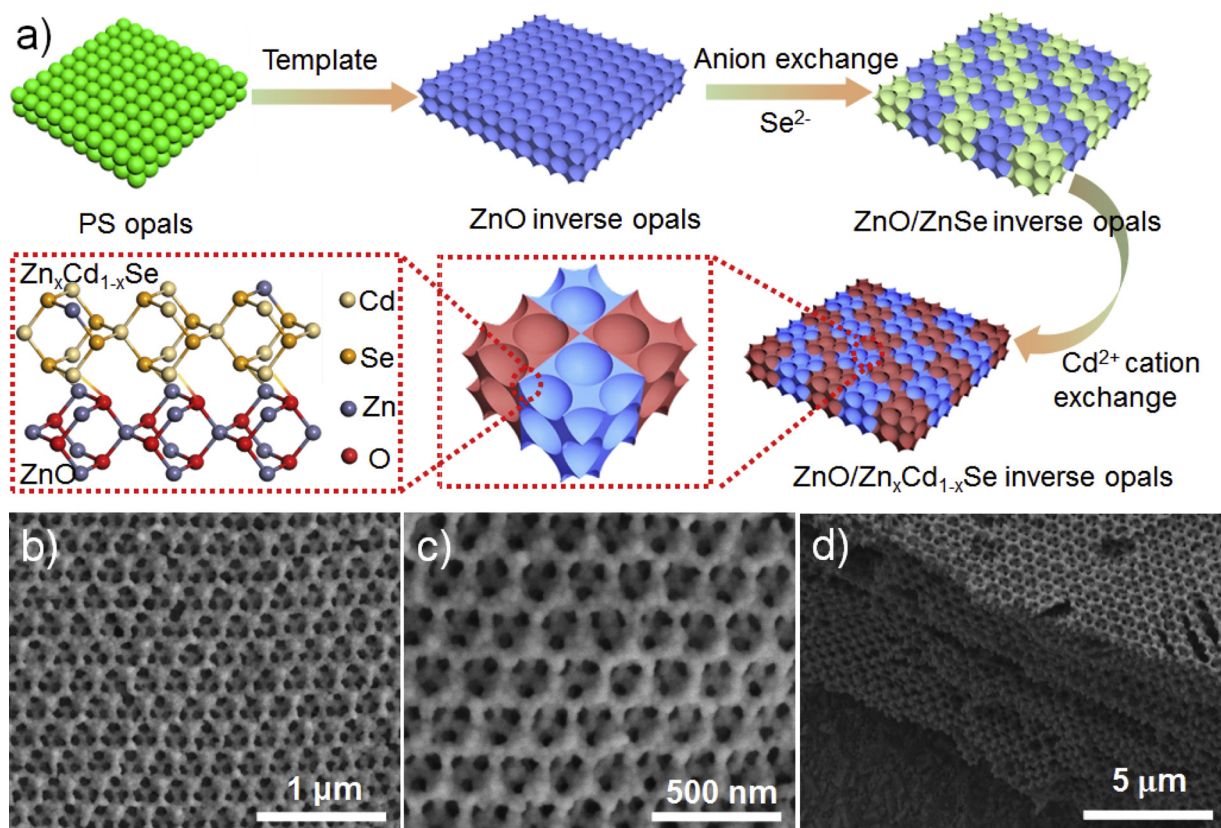


**Fig. 1.** (a) Schematic illustration of the formation process of the 3DOM  $\text{ZnO}/\text{Zn}_x\text{Cd}_{1-x}\text{Se}$  inverse opal, (b, c) Top view, and (d) Cross-sectional SEM images of the as-prepared typical 3DOM  $\text{ZnO}/\text{Zn}_x\text{Cd}_{1-x}\text{Se}$  inverse opal.

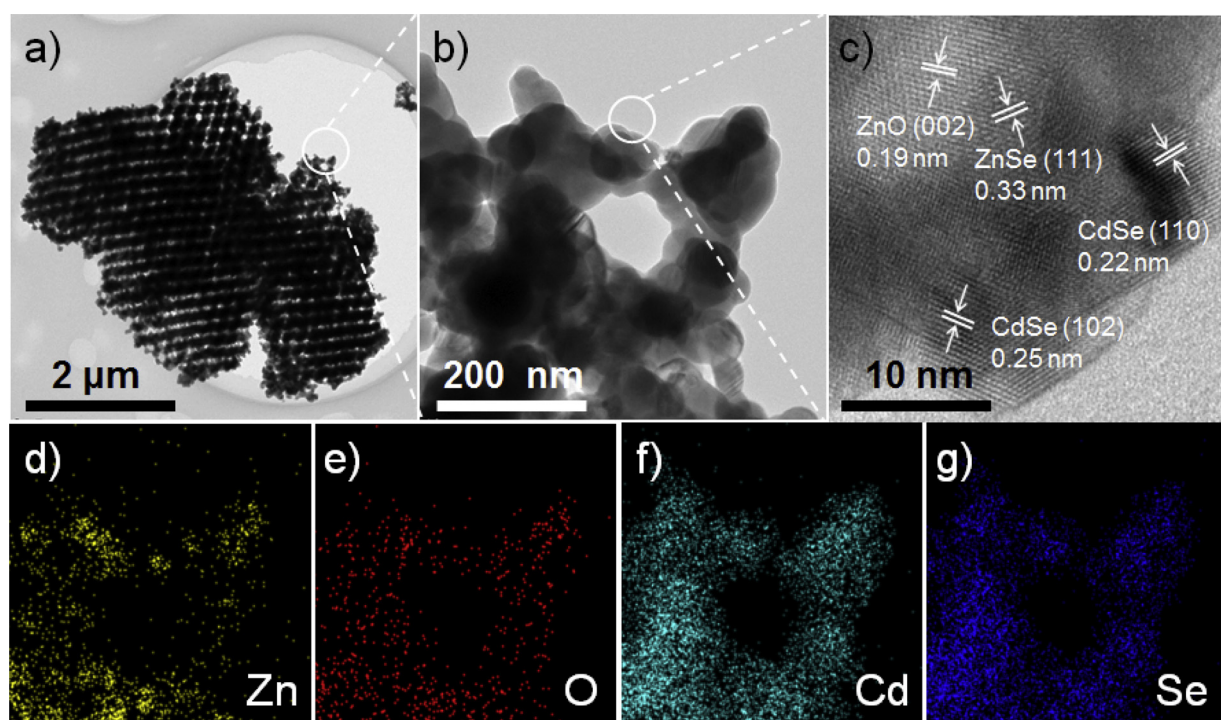


**Fig. 2.** (a–b) TEM graphs with different magnifications, (c) High-resolution TEM graph, and (d–g) Elemental mapping images of Zn (yellow), O (red), Cd (cyan) and Se (blue) from the same area of the as-prepared typical 3DOM  $\text{ZnO}/\text{Zn}_x\text{Cd}_{1-x}\text{Se}$  inverse opal (For interpretation of the references to colour in this figure legend, the reader is referred to the web version of this article).

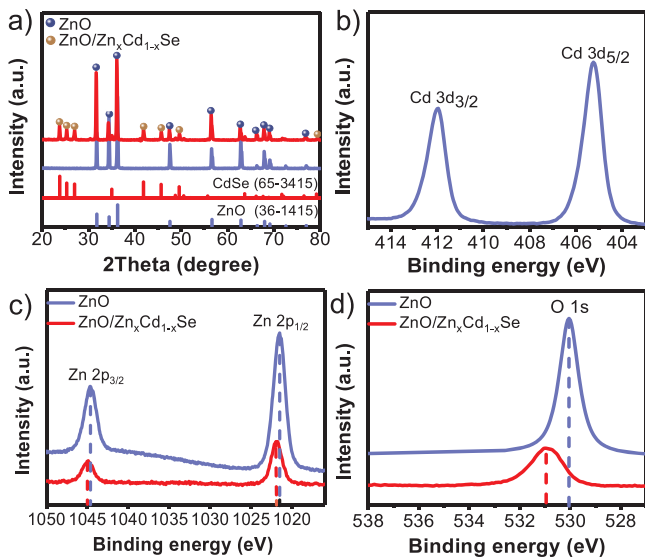


Fig. 3. (a) XRD pattern, XPS core level of Cd 3d (b), Zn 2p (c) and O 1s (d) of the as-prepared 3DOM ZnO and ZnO/Zn<sub>x</sub>Cd<sub>1-x</sub>Se inverse opals.

and Figure S8, a steep absorption edge at 390 nm was observed in ZnO inverse opal, which is consistent with the wide bandgap of ZnO (3.2 eV). With regard to ZnO/Zn<sub>x</sub>Cd<sub>1-x</sub>Se inverse opal, due to the narrow bandgap of Zn<sub>x</sub>Cd<sub>1-x</sub>Se, the sample displayed red shifts in the bandgap transition (1.82 eV) and an enhanced absorption in the visible-light region. As displayed in Fig. 4d, the light harvesting efficiency of the 3DOM ZnO/Zn<sub>x</sub>Cd<sub>1-x</sub>Se inverse opal is in the range of 80.63–94.0% in the wavelength range of 400–700 nm, an obvious enhancement as compared with the 3DOM ZnO inverse opal. It suggests that growth of Zn<sub>x</sub>Cd<sub>1-x</sub>Se shell layer on ZnO skeleton is helpful to harvest the visible photons.

PEC performances of the as-prepared 3DOM ZnO/Zn<sub>x</sub>Cd<sub>1-x</sub>Se samples were evaluated under simulated sunlight in a three-electrode system. The LSV curves of the different photoanodes measured under

AM 1.5 G solar light irradiation (100 mW cm<sup>-2</sup>) are presented in Fig. 5a with negligible current density measured under dark conditions. As seen, the saturated photocurrent density of the bare 3DOM ZnO inverse opal photoanode is less than 1 mA cm<sup>-2</sup> at 1.23 V vs. RHE. Such a low photocurrent density could be attributed to the high levels of recombination of photogenerated charges and low visible light photon harvesting. After growth of CdSe shell layer, the onset potential is negatively shifted and the saturated photocurrent density of the 3DOM ZnO/Zn<sub>x</sub>Cd<sub>1-x</sub>Se photoanode reached 24.77 mA cm<sup>-2</sup> at 1.23 V versus RHE, which represents an almost 25 times increase in the current density compared with the pristine ZnO photoanode. The achieved photocurrent density value is also superior to most of the previous reported results in quantum dots sensitized photoelectrodes, such as CdSe/RGO/Au co-sensitized ZnO nanorod (10.74 mA cm<sup>-2</sup>) [35], CdSe sensitized ZnO nanorod (14.9 mA cm<sup>-2</sup>) [36], CdSe sensitized ZnO/ZnSe nanocables arrays (13.57 mA cm<sup>-2</sup>) [37], and CdSe/CdS sensitized ZnO nanotube arrays (20.03 mA cm<sup>-2</sup>) [38]. Detailed comparisons can be easily found from Table S1. This remarkable enhancement in PEC performance could be ascribed to the advantageous features offered by the unique 3DOM ZnO/Zn<sub>x</sub>Cd<sub>1-x</sub>Se inverse opal, such as boosts the visible light absorption, type-II band alignment benefits the separation of photogenerated carriers, and construction of the binder-free interface heterojunction. In order to discover the contribution of visible light to the enhancement of photocurrent density, the LSV curves of the as-prepared photoanodes under the visible light are exhibited in Fig. 5b. The saturated photocurrent density of the 3DOM ZnO/Zn<sub>x</sub>Cd<sub>1-x</sub>Se photoanode is still as high as 15.83 mA cm<sup>-2</sup>, as compared to the 3DOM ZnO photoanode is only 0.15 mA cm<sup>-2</sup> at 1.23 V versus RHE under the cutoff 400 nm wavelength light.

Fig. 5c shows the photoresponses of the as-prepared photoanodes over time at 1.23 V vs. RHE with chopped light illumination. It can be seen that the photo-current stabilized at 17.63 mA cm<sup>-2</sup> once the light was switched on, suggesting rapid transfer of the photogenerated electrons from Zn<sub>x</sub>Cd<sub>1-x</sub>Se shell to ZnO skeleton. In addition, once the light was switched off, the photocurrent decayed rapidly to negligible dark current, indicating fast transport of photo-generated electrons from the ZnO skeleton to the FTO substrate. Generally, the

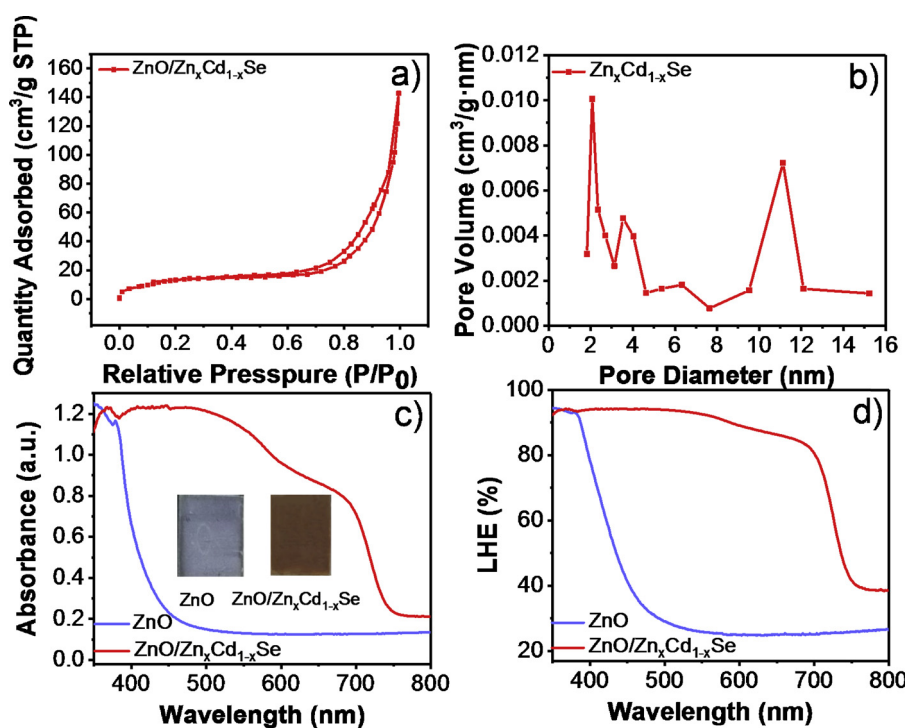
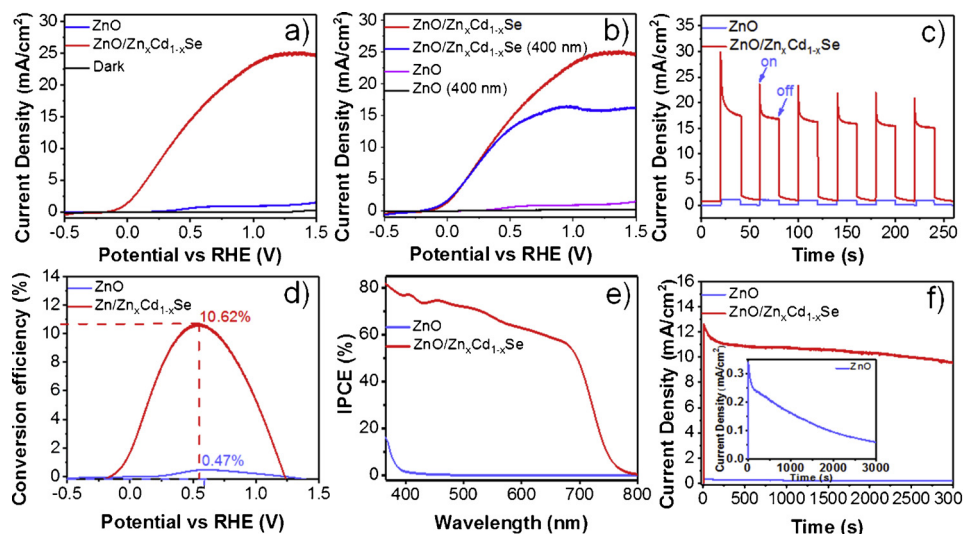


Fig. 4. (a) Diffuse reflectance spectra, (b) Light harvesting efficiency of the as-prepared 3DOM ZnO and ZnO/Zn<sub>x</sub>Cd<sub>1-x</sub>Se inverse opals.



**Fig. 5.** (a) LSV curves under AM 1.5 G simulated sunlight, (b) cut off 400 nm at a scan rate of  $10 \text{ mV s}^{-1}$ , (c) Amperometric I – t curves under chopped light irradiation with on/off interval of 20 s at 1.23 V vs RHE, (d) Photoconversion efficiency curves, (e) Incident-photon-to-current conversion efficiency spectra, and (f) Steady-state photocurrents under continuous illumination at an applied potential 1.23 V vs RHE of the as-prepared 3DOM ZnO and  $\text{ZnO/Zn}_x\text{Cd}_{1-x}\text{Se}$  inverse opals.

photocurrent spikes in the beginning of switching can be attributed to instantaneous separation of photogenerated electron-hole pairs and subsequent charge recombination at the photoanode surface. After the generation rate and recombination rate attain equilibrium, a steady-state photocurrent density is achieved [39,40]. The transient spike might imply the presence of surface defects on the 3DOM  $\text{ZnO/Zn}_x\text{Cd}_{1-x}\text{Se}$  photoanode for charge recombination.

To obtain the optimum thickness of CdSe shell, 3DOM  $\text{ZnO/Zn}_x\text{Cd}_{1-x}\text{Se}$  inverse opals with varied ion exchange conditions were carried out. As shown in Figure S6, the photocurrent density first increases with increasing CdSe amount, reaching a maximum value, and then decreases. Initially, the amount of CdSe on the surface of ZnO skeleton increases with the reaction precursors, leading to better visible-light absorption and thus more efficient exciton generation. However, if the precursor concentration is too high, an excessive amount of CdSe may deposited on ZnO inverse opal skeleton (Figure S7), which blocks the micropores of the inverse opal, increases the charge diffusion distance, and results in decreasing photocurrent density. As a result, the optimized reaction system would be contained around 0.025 M  $\text{CdCl}_2$  and 0.025 M Se powers found to be suitable for the growth of CdSe shell.

Fig. 5d showed the photoconversion efficiency of the 3DOM  $\text{ZnO/Zn}_x\text{Cd}_{1-x}\text{Se}$  inverse opal photoanodes, which suggested that the 3DOM  $\text{ZnO/Zn}_x\text{Cd}_{1-x}\text{Se}$  inverse opal exhibited much higher photoconversion efficiency than that of the pristine ZnO inverse opal. The photoconversion efficiency of the optimized 3DOM  $\text{ZnO/Zn}_x\text{Cd}_{1-x}\text{Se}$  inverse opal achieved as high as 10.64% at an applied potential of 0.52 V versus RHE, an about 22.63 times increase relative to that of the pristine ZnO inverse opal (0.47% at 0.61 V versus RHE). To our best knowledge, it is the highest value that has been reported for CdSe sensitized ZnO, and/or  $\text{ZnO/ZnSe}$  nanostructures. Furthermore, the incident-photon-to-current conversion efficiency (IPCE) spectra for the 3DOM  $\text{ZnO/Zn}_x\text{Cd}_{1-x}\text{Se}$  inverse opal photoanodes were measured, which are shown in Fig. 5e. Obviously, the optimized 3DOM  $\text{ZnO/Zn}_x\text{Cd}_{1-x}\text{Se}$  inverse opal exhibited considerably higher photoactivity than that of the pristine ZnO in the whole range from 350 nm to 800 nm. The IPCE was as high as 60.0–82.5% at the wavelength of 350–700 nm, which could be attributed to enhanced light absorption, facilitated charge separation, and efficient charge transport offered by the 3DOM  $\text{ZnO/Zn}_x\text{Cd}_{1-x}\text{Se}$  inverse opal with binder-free heterojunction. This enhancement of the IPCE is in agreement with the distribution of the UV–vis diffuse reflectance spectra.

The photostability of the optimized 3DOM  $\text{ZnO/Zn}_x\text{Cd}_{1-x}\text{Se}$  inverse opal was also investigated by the I-t curves. As shown in Fig. 5f, the photocurrent generated by the bare 3DOM ZnO inverse opal decreased significantly with a photocurrent density decay of 86.8% by 3000 s

illumination, indicating that photogenerated holes accumulated at the surface of ZnO due to poor kinetics for water splitting. In contrast, the optimized 3DOM  $\text{ZnO/Zn}_x\text{Cd}_{1-x}\text{Se}$  inverse opal photoanode maintain 82.6% initial photocurrent density of  $12.12 \text{ mA cm}^{-2}$  within 3000 s illumination, indicating that heteroepitaxial growth of CdSe shell on ZnO skeleton surface greatly improved the photostability in the electrolyte solution. The 3DOM  $\text{ZnO/Zn}_x\text{Cd}_{1-x}\text{Se}$  inverse opal provides the binder-free heterojunction, type-II band alignment and the shorten charge diffusion distance, which improve the charge transfer, and accelerate the electrode/electrolyte surface redox kinetics.

Hydrogen evolution is further used to evaluate the stability of the as-prepared photoanodes. As illustrated in Fig. 6a, the evolution rate of  $\text{H}_2$  from the 3DOM ZnO, and  $\text{ZnO/Zn}_x\text{Cd}_{1-x}\text{Se}$  inverse opal photoanodes were  $6.0$  and  $148.0 \mu\text{mol cm}^{-2} \text{ h}^{-1}$  in a hole sacrificial reagent circumstance, respectively. It is seldom reported for the CdSe-based materials for a long time PEC water splitting without any protective coating layer. Moreover, as shown in Fig. 6b, the optimized 3DOM  $\text{ZnO/Zn}_x\text{Cd}_{1-x}\text{Se}$  inverse opal photoanode exhibits a high Faradaic efficiency of ca. 95.0% under the 150 min illumination. However, the Faradaic efficiency of pristine ZnO photoanode gradually decrease from 85% to 45% during the reaction period. Thus, the optimized 3DOM  $\text{ZnO/Zn}_x\text{Cd}_{1-x}\text{Se}$  inverse opal exhibits a high performance in water splitting because (i) the 3DOM inverse opal structure offers a large surface area for contact with electrolyte; (ii) the type-II band alignment facilitates charge diffusion; (iii) the binder-free heterojunction interface raps carrier transfer; and (iv) the heteroepitaxial growth of CdSe shell boosts the visible light absorption for PEC water splitting.

To investigate the charge transfer of the 3DOM  $\text{ZnO/Zn}_x\text{Cd}_{1-x}\text{Se}$  inverse opal photoanode, electrochemical impedance spectroscopy measurements were carried out covering the frequency range of  $10^4$ –0.1 Hz using an amplitude of  $10 \text{ mV}$  at open-circuit condition

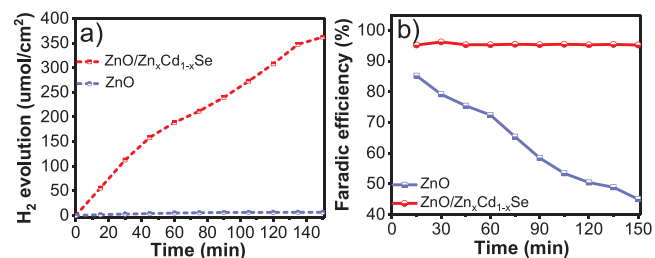


**Fig. 6.** (a)  $\text{H}_2$  gas evolution curves, (b) Faradic efficiency curves of the as-prepared 3DOM ZnO and  $\text{ZnO/Zn}_x\text{Cd}_{1-x}\text{Se}$  inverse opals at 1.23 V versus RHE under AM 1.5 G for different times.

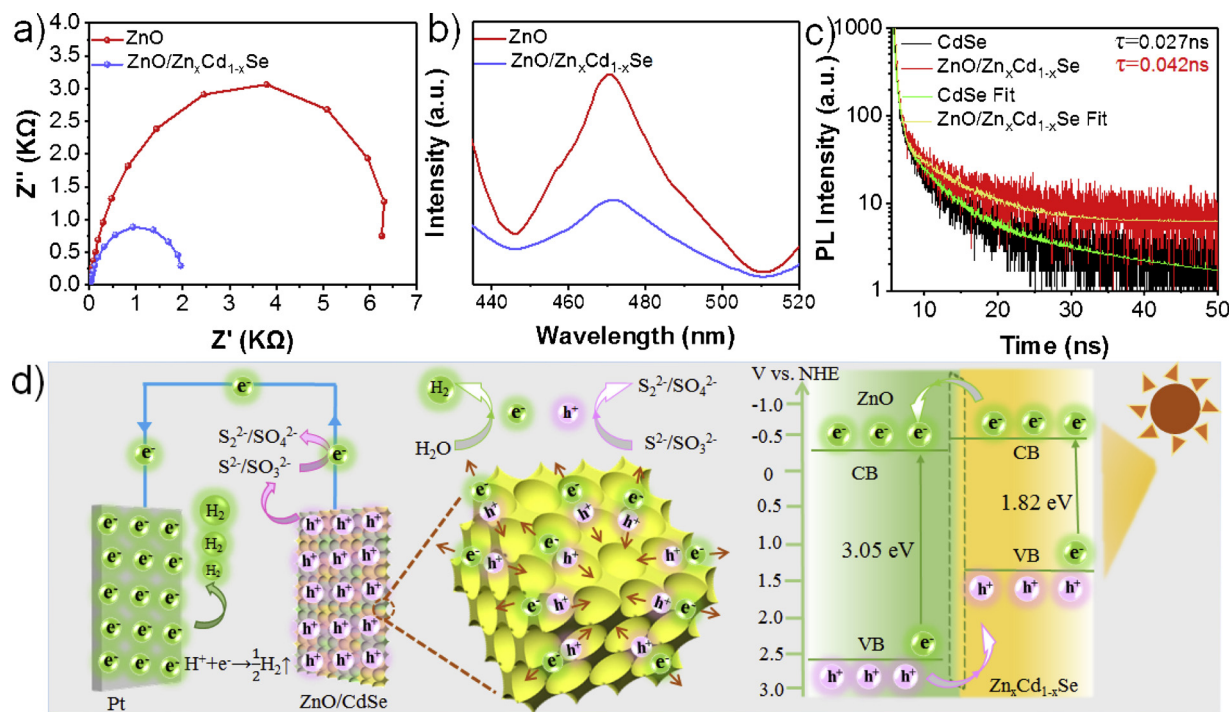


**Fig. 7.** (a) Electrochemical impedance spectra, (b) Photoluminescence spectra, (c) Time-resolved photoluminescence decay spectra, and (d) Schematic diagram of PEC water splitting and charge transfer process for the as-prepared 3DOM ZnO and ZnO/Zn<sub>x</sub>Cd<sub>1-x</sub>Se inverse opal photoanodes.

under simulated light. The Nyquist plots of the obtained EIS data are shown in Fig. 7a. Compared with the pristine ZnO sample, the arc radius of 3DOM ZnO/Zn<sub>x</sub>Cd<sub>1-x</sub>Se inverse opal electrode is greatly reduced, indicating that the 3DOM architecture with binder-free heterojunction interface can elevate the interfacial charge transfer and reduce the interfacial reaction resistance, which would greatly promote the electron–hole separation. Photoluminescence (PL) spectra and time-resolved PL decay spectra measurements of the 3DOM ZnO, ZnO/Zn<sub>x</sub>Cd<sub>1-x</sub>Se inverse opals were performed. As shown in Fig. 7b, the PL intensity of the 3DOM ZnO/Zn<sub>x</sub>Cd<sub>1-x</sub>Se inverse opal was much lower than the pristine ZnO inverse opal. This decrease can be explained by enhanced PL quenching because of the facilitated electron transfer from Zn<sub>x</sub>Cd<sub>1-x</sub>Se to ZnO by the binder-free heterojunction interface and favorable conduction band offset, which was beneficial to PEC water splitting [41]. To better understand the charge transfer between Zn<sub>x</sub>Cd<sub>1-x</sub>Se shell and ZnO skeleton, the time-resolved PL spectra of CdSe and ZnO/Zn<sub>x</sub>Cd<sub>1-x</sub>Se inverse opal were also investigated. As shown in Fig. 7c, an increase in average lifetime was observed in the case of ZnO/Zn<sub>x</sub>Cd<sub>1-x</sub>Se inverse opal ( $42 \times 10^{-3}$  ns), which was longer than that of pure CdSe ( $27 \times 10^{-3}$  ns). Therefore, the EIS and PL results suggested that the 3DOM ZnO/Zn<sub>x</sub>Cd<sub>1-x</sub>Se inverse opal had faster charge transfer at the Zn<sub>x</sub>Cd<sub>1-x</sub>Se/electrolyte interface and from ZnO to the FTO substrate.

According to the above experimental results and the Mott–Schottky analysis (Figure S9), the charge separation and transfer processes in the as-prepared 3DOM ZnO/Zn<sub>x</sub>Cd<sub>1-x</sub>Se inverse opal photoanode are schematically illustrated in Fig. 7d. As seen, Zn<sub>x</sub>Cd<sub>1-x</sub>Se is easy to harvest the visible light because of the narrow bandgap, and the ultraviolet light can be trapped by ZnO under illumination. The photogenerated electrons were instantaneously excited from VB (1.32 V) of Zn<sub>x</sub>Cd<sub>1-x</sub>Se to CB (-0.5 V) and then rapidly transferred to the CB (-0.38 V) of ZnO because of the favorable band alignment and low interfacial resistance between Zn<sub>x</sub>Cd<sub>1-x</sub>Se and ZnO. The high electron mobility of the ZnO skeleton was helpful for the transfer of the electrons to the current collector, which were then transported to the Pt electrode to generate hydrogen. Meanwhile, the photogenerated holes flowed to the surfaces of the Zn<sub>x</sub>Cd<sub>1-x</sub>Se shell where the oxidation reaction occurred. In such a

way, the photoexcited electrons and holes in the 3DOM ZnO/Zn<sub>x</sub>Cd<sub>1-x</sub>Se inverse opal can be separated efficiently.

#### 4. Conclusions

In summary, 3DOM ZnO/Zn<sub>x</sub>Cd<sub>1-x</sub>Se inverse opals with binder-free heterojunction interface have been successfully fabricated by combining colloidal spheres template, and subsequent ion exchange reactions. The large surface area, favorable band alignment, and low interfacial resistance contribute to the effective separation of photogenerated electron–hole pairs and transportation of the electrons to the electrode surface, and thus leading to a significantly enhanced PEC performance of the 3DOM ZnO/Zn<sub>x</sub>Cd<sub>1-x</sub>Se inverse opal. Our results suggest that a high electron mobility nanostructured host skeleton designed with tailored constitutes is an effective strategy to boost the overall PEC performances. This strategy may also be applied to development of new hybrid material systems with advanced nanostructures for superior PEC applications.

#### Acknowledgements

This work was supported by the National Natural Science Foundation of China (21771001, 21671001), the Anhui Provincial Natural Science Foundation (1708085ME120), the Key Natural Science Research Project of the Anhui Provincial Education Department (KJ2017A007), the Program of Anhui Scientific and Technical Leaders Reserve Candidates (2018H168), the Scholar Program for the Outstanding Innovative Talent of College Discipline (Specialty), the Key Lab of Photovoltaic and Energy Conservation Materials, Chinese Academy of Science (PECL2018KF007), the Research Fund Program of Guangdong Provincial Key Laboratory of Environmental Pollution Control and Remediation Technology (2018K11), and open fund for Discipline Construction, Institute of Physical Science and Information Technology, Anhui University.

## Appendix A. Supplementary data

Supplementary material related to this article can be found, in the online version, at doi:<https://doi.org/10.1016/j.apcatb.2019.01.011>.

## References

- [1] X. Chen, L. Liu, P.Y. Yu, S.S. Mao, Increasing solar absorption for photocatalysis with black hydrogenated titanium dioxide nanocrystals, *Science* 331 (2011) 746–750.
- [2] G. Zhang, G. Liu, L. Wang, J.T. Irvine, Inorganic perovskite photocatalysts for solar energy utilization, *Chem. Soc. Rev.* 45 (2016) 5951–5984.
- [3] Y. Shi, B. Zhang, Recent advances in transition metal phosphide nanomaterials: synthesis and applications in hydrogen evolution reaction, *Chem. Soc. Rev.* 45 (2016) 1529–1541.
- [4] J.L. Young, M.A. Steiner, H. Dösscher, R.M. France, J.A. Turner, Todd G. Deutsch, Direct solar-to-hydrogen conversion via inverted metamorphic multi-junction semiconductor architectures, *Nat. Energy* 2 (2017) 17028.
- [5] S. Hu, C. Xiang, S. Haussener, A.D. Berger, N.S. Lewis, An analysis of the optimal band gaps of light absorbers in integrated tandem photoelectrochemical water-splitting systems, *Energy Environ. Sci.* 6 (2013) 2984.
- [6] J. Jia, L.C. Seitz, J.D. Benck, Y. Huo, Y. Chen, J.W. Ng, T. Bilir, J.S. Harris, T.F. Jaramillo, Solar water splitting by photovoltaic-electrolysis with a solar-to-hydrogen efficiency over 30%, *Nat. Commun.* 7 (2016) 13237.
- [7] H. Park, H.-i. Kim, G.-h. Moon, W. Choi, Photoinduced charge transfer processes in solar photocatalysis based on modified TiO<sub>2</sub>, *Energy Environ. Sci.* 9 (2016) 411–433.
- [8] Y. Chang, K. Yu, C. Zhang, Z. Yang, Y. Feng, H. Hao, Y. Jiang, L.-L. Lou, W. Zhou, S. Liu, Ternary CdS/Au/3DOM-SrTiO<sub>3</sub> composites with synergistic enhancement for hydrogen production from visible-light photocatalytic water splitting, *Appl. Catal. B* 215 (2017) 74–84.
- [9] T. Yang, J. Xue, H. Tan, A. Xie, S. Li, W. Yan, Y. Shen, Highly ordered ZnO/ZnFe<sub>2</sub>O<sub>4</sub> inverse opals with binder-free heterojunction interfaces for high-performance photoelectrochemical water splitting, *J. Mater. Chem. A Mater. Energy Sustain.* 6 (2018) 1210–1218.
- [10] M. Zalfani, Z.-Y. Hu, W.-B. Yu, M. Mahdouani, R. Bourguiga, M. Wu, Y. Li, G. Van Tendeloo, Y. Djaoued, B.-L. Su, BiVO<sub>4</sub>/3DOM TiO<sub>2</sub> nanocomposites: effect of BiVO<sub>4</sub> as highly efficient visible light sensitizer for highly improved visible light photocatalytic activity in the degradation of dye pollutants, *Appl. Catal. B* 205 (2017) 121–132.
- [11] M. Srinivasarao, D. Collings, A. Philips, S. Patel, Three-dimensionally ordered array of air bubbles in a polymer film, *Science* 292 (2001) 79–83.
- [12] A. Stein, B.E. Wilson, S.G. Rudisill, Design and functionality of colloidal-crystal-templated materials—chemical applications of inverse opals, *Chem. Soc. Rev.* 42 (2013) 2763–2803.
- [13] C. Ding, J. Shi, Z. Wang, C. Li, Photoelectrocatalytic water splitting: significance of cocatalysts, electrolyte, and interfaces, *ACS Catal.* 7 (2016) 675–688.
- [14] J. Su, L. Guo, N. Bao, C.A. Grimes, Nanostructured WO<sub>3</sub>/BiVO<sub>4</sub> heterojunction films for efficient photoelectrochemical water splitting, *Nano Lett.* 11 (2011) 1928–1933.
- [15] M. Ma, J.K. Kim, K. Zhang, X. Shi, S.J. Kim, J.H. Moon, J.H. Park, Double-deck inverse opal photoanodes: efficient light absorption and charge separation in heterojunction, *Chem. Mater.* 26 (2014) 5592–5597.
- [16] J. Hou, C. Yang, H. Cheng, S. Jiao, O. Takeda, H. Zhu, High-performance p-Cu<sub>2</sub>O/n-TaON heterojunction nanorod photoanodes passivated with an ultrathin carbon sheath for photoelectrochemical water splitting, *Energy Environ. Sci.* 7 (2014) 3758–3768.
- [17] B. Zhang, Z. Wang, B. Huang, X. Zhang, X. Qin, H. Li, Y. Dai, Y. Li, Anisotropic photoelectrochemical (PEC) performances of ZnO single-crystalline photoanode: effect of internal electrostatic fields on the separation of photogenerated charge carriers during PEC water splitting, *Chem. Mater.* 28 (2016) 6613–6620.
- [18] M. Wu, W.J. Chen, Y.H. Shen, F.Z. Huang, C.H. Li, S.K. Li, In situ growth of matchlike ZnO/Au plasmonic heterostructure for enhanced photoelectrochemical water splitting, *ACS Appl. Mater. Interfaces* 6 (2014) 15052–15060.
- [19] A. Wolcott, W.A. Smith, T.R. Kuykendall, Y. Zhao, J.Z. Zhang, Photoelectrochemical study of nanostructured ZnO thin films for hydrogen generation from water splitting, *Adv. Funct. Mater.* 19 (2009) 1849–1856.
- [20] Z. Bai, X. Yan, Y. Li, Z. Kang, S. Cao, Y. Zhang, 3D-Branched ZnO/CdS nanowire arrays for solar water splitting and the service safety research, *Adv. Funct. Mater.* 6 (2016) 1501459.
- [21] C.X. Guo, J. Xie, H. Yang, C.M. Li, Au@CdS core-shell nanoparticles-modified ZnO nanowires photoanode for efficient photoelectrochemical water splitting, *Adv. Sci.* 2 (2015) 1500135.
- [22] R. Zhang, Q.P. Luo, H.Y. Chen, X.Y. Yu, D.B. Kuang, C.Y. Su, CdS/CdSe quantum dot shell decorated vertical ZnO nanowire arrays by spin-coating-based SILAR for photoelectrochemical cells and quantum-dot-sensitized solar cells, *ChemPhysChem* 13 (2012) 1435–1439.
- [23] J. Miao, H.B. Yang, S.Y. Khoo, B. Liu, Electrochemical fabrication of ZnO-CdSe core-shell nanorod arrays for efficient photoelectrochemical water splitting, *Nanoscale* 5 (2013) 11118–11124.
- [24] H.M. Chen, C.K. Chen, Y.C. Chang, C.W. Tsai, R.S. Liu, S.F. Hu, W.S. Chang, K.H. Chen, Quantum dot monolayer sensitized ZnO nanowire-array photoelectrodes: true efficiency for water splitting, *Angew. Chem.* 49 (2010) 5966–5969.
- [25] R. Bera, A. Dutta, S. Kundu, V. Polshettiwar, A. Patra, Design of a CdS/CdSe heterostructure for efficient H<sub>2</sub> generation and photovoltaic applications, *J. Phys. Chem. C* 122 (2018) 12158–12167.
- [26] G. Wang, X. Yang, F. Qian, J.Z. Zhang, Y. Li, Double-sided CdS and CdSe quantum dot co-sensitized ZnO nanowire arrays for photoelectrochemical hydrogen generation, *Nano Lett.* 10 (2010) 1088–1092.
- [27] N. Chouhan, C.L. Yeh, S.F. Hu, R.S. Liu, W.S. Chang, K.H. Chen, Photocatalytic CdSe QDs-decorated ZnO nanotubes: an effective photoelectrode for splitting water, *Chem. Commun. (Camb.)* 47 (2011) 3493–3495.
- [28] X. She, Z. Zhang, M. Baek, M. Choi, K. Yong, J. Wang, Q. Xue, Recycling rare-earth slag for enhanced photoelectrochemical efficiency of a reduced graphene oxide-covered CdSe@ZnO hetero-nanostructured photoanode, *ChemElectroChem* 3 (2016) 1890–1898.
- [29] F. Qiu, Z. Han, J.J. Peterson, M.Y. Odoi, K.L. Sowers, T.D. Krauss, Photocatalytic hydrogen generation by CdSe/CdS Nnanoparticles, *Nano Lett.* 16 (2016) 5347–5352.
- [30] C. Tan, H. Zhang, Epitaxial growth of hetero-nanostructures based on ultrathin two-dimensional nanosheets, *J. Am. Chem. Soc.* 137 (2015) 12162–12174.
- [31] L. Hou, L. Lian, L. Zhang, G. Pang, C. Yuan, X. Zhang, Self-sacrifice template fabrication of hierarchical mesoporous bi-component-active ZnO/ZnFe<sub>2</sub>O<sub>4</sub> sub-microcubes as superior anode towards high-performance lithium-ion battery, *Adv. Funct. Mater.* 25 (2015) 238–246.
- [32] X. Wang, W. Song, B. Liu, G. Chen, D. Chen, C. Zhou, G. Shen, High-performance organic-inorganic hybrid photodetectors based on P<sub>3</sub>HT:CdSe nanowire heterojunctions on rigid and flexible substrates, *Adv. Funct. Mater.* 23 (2013) 1202–1209.
- [33] Z. Song, B. Hong, X. Zhu, F. Zhang, S. Li, J. Ding, X. Jiang, J. Bao, C. Gao, S. Sun, CdS/Au/Ti/Pb(Mg<sub>1/3</sub>Nb<sub>2/3</sub>)<sub>0.7</sub>Ti<sub>0.3</sub>O<sub>3</sub> photocatalysts and biphotoelectrodes with ferroelectric polarization in single domain for efficient water splitting, *Appl. Catal. B* 238 (2018) 248–254.
- [34] K. Zarębska, T. Łęcki, M. Skompska, Synthesis of CdSe on FTO-supported ZnO nanorods by SILAR and electrochemical methods and comparison of photoelectrochemical properties of FTO/ZnO/CdSe systems in aqueous S<sup>2-</sup>/Sn<sup>2-</sup> electrolyte, *J. Electroanal. Chem. (Lausanne)* 819 (2018) 459–468.
- [35] Z. Zhang, M. Choi, M. Baek, Z. Deng, K. Yong, Plasmonic and passivation effects of Au decorated RGO@CdSe nanofilm uplifted by CdSe@ZnO nanorods with photoelectrochemical enhancement, *Nano Energy* 21 (2016) 185–197.
- [36] J. Miao, H.B. Yang, S.Y. Khoo, B. Liu, Electrochemical fabrication of ZnO-CdSe core-shell nanorod arrays for efficient photoelectrochemical water splitting, *Nanoscale* 5 (2013) 11118–11124.
- [37] J. Xu, X. Yang, Q.-D. Yang, T.-L. Wong, S.-T. Lee, W.-J. Zhang, C.-S. Lee, Arrays of CdSe sensitized ZnO/ZnSe nanocables for efficient solar cells with high open-circuit voltage, *J. Mater. Chem.* 22 (2012) 13374.
- [38] P.Y. Kuang, Y.Z. Su, K. Xiao, Z.Q. Liu, N. Li, H.J. Wang, J. Zhang, Double-shelled CdS and CdSe co-sensitized ZnO porous nanotube arrays for superior photoelectrocatalytic applications, *ACS Appl. Mater. Interfaces* 7 (2015) 16387–16394.
- [39] W. Wang, C. Jin, L. Qi, Hierarchical CdS nanorod@SnO<sub>2</sub> nanobowl arrays for efficient and stable photoelectrochemical hydrogen generation, *Small* (2018) 1801352.
- [40] J. Song, M.J. Seo, T.H. Lee, Y.-R. Jo, J. Lee, T.L. Kim, S.-Y. Kim, S.-M. Kim, S.Y. Jeong, H. An, S. Kim, B.H. Lee, D. Lee, H.W. Jang, B.-J. Kim, S. Lee, Tailoring crystallographic orientations to substantially enhance charge separation efficiency in anisotropic BiVO<sub>4</sub> photoanodes, *ACS Catal.* 8 (2018) 5952–5962.
- [41] M. Zhong, T. Hisatomi, Y. Kuang, J. Zhao, M. Liu, A. Iwase, Q. Jia, H. Nishiyama, T. Minegishi, M. Nakabayashi, N. Shibata, R. Niishiro, C. Katayama, H. Shibano, M. Katayama, A. Kudo, T. Yamada, K. Domen, Surface modification of CoOx loaded BiVO<sub>4</sub> photoanodes with ultrathin p-Type NiO layers for improved solar water oxidation, *J. Am. Chem. Soc.* 137 (2015) 5053–5060.